

# Unsteady hydrodynamics of a full-scale tidal turbine operating in large wave conditions

Gabriel Thomas Scarlett<sup>a</sup>, Brian Sellar<sup>a</sup>, Ton van den Bremer<sup>a,b</sup>, Ignazio Maria Viola<sup>a,\*</sup>

<sup>a</sup>*School of Engineering, Institute for Energy Systems, The University of Edinburgh, Edinburgh, EH9 3DW*

<sup>b</sup>*Department of Engineering, University of Oxford, Oxford, OX1 3PJ*

---

## Abstract

We develop a model which couples dynamic stall, rotational augmentation and blade-element momentum theory to analyse the unsteady flow around and loads acting on a tidal turbine rotor. This is implemented in a MATLAB code freely available on GitHub. The formulation and implementation of the model is explained herein. The blade-element momentum implementation has been validated using AeroDyn an opensource software from the National Renewable Energy Laboratory. The dynamic stall module has been validated against experimental data for the non-rotating case. For the coupling of dynamic stall with rotational augmentation a quantitative validation was carried out comparing results from the NREL Phase VI experiment.

---

---

\*Corresponding author

Email address: I.M.Viola@ed.ac.uk (Ignazio Maria Viola)

## Nomenclature

$a$	Axial induction factor (-)	$R_h$	Blade hub radius (m)
$a'$	Tangential induction factor (-)	$s$	Reduced time (-)
$AR$	Aspect ratio (-)	$T$	Thrust force acting on actuator disc (N)
$B$	Geometry constant (-)	$t$	Time (s)
$b_1$	Rotational constant (-)	$T_r$	Period of rotation (s)
$b_2$	Rotational constant (-)	$T_v$	Vortex time lag constant (-)
$c$	Chord length (m)	$T_\alpha$	Angle time lag constant (-)
$C_L^p$	Lift coefficient in attached flow (-)	$T_{vL}$	Vortex transit time (-)
$C_C^u$	Unsteady chordwise force coefficient (-)	$U_0$	Freestream reference velocity ( $\text{ms}^{-1}$ )
$C_D^u$	Unsteady coefficient (-)	$U_\psi$	Tangential velocity to blade ( $\text{ms}^{-1}$ )
$C_N^u$	Unsteady normal force coefficient (-)	$U_x$	Streamwise velocity ( $\text{ms}^{-1}$ )
$C_N^v$	Vortex normal force coefficient (-)	$U_z$	Depthwise velocity ( $\text{ms}^{-1}$ )
$C_D^{ind}$	Induced drag coefficient (-)	$V_x$	Vortex shape function (-)
$C_D^{st}$	Static drag coefficient (-)	$W$	Relative inflow velocity ( $\text{ms}^{-1}$ )
$C_D^{vis}$	Viscous drag coefficient (-)	$x$	Horizontal Cartesian coordinate (m)
$C_D$	Drag coefficient (-)	$y$	Horizontal Cartesian coordinate (m)
$C_L$	Lift coefficient (-)	$z$	Vertical Cartesian coordinate (m)
$C_N$	Normal force coefficient (-)	$z_0$	Depth of rotor hub (m)
$C_P$	Power coefficient (-)	$\alpha$	Angle of attack (rad)
$C_Q$	Torque coefficient (-)	$\alpha'$	Lagged angle of attack (rad)
$C_T$	Thrust coefficient (-)	$\alpha^{rot}$	Rotational angle of attack (rad)
$C_{D_0}$	Zero lift drag coefficient (-)	$\alpha_0$	Angle of zero lift (rad)
$C_D^{rot}$	Rotational drag coefficient (-)	$\alpha_{cr}$	Critical angle (rad)
$C_{F_{Tan}}$	Tangential force coefficient (-)	$\alpha_{ds0}$	Critical dynamic stall onset angle (rad)
$C_{F_T}$	Thrust force coefficient (-)	$\alpha_{ds}$	Angle of dynamic stall onset (rad)
$C_L^u$	Unsteady lift coefficient (-)	$\alpha_{ss}$	Angle of static stall (rad)
$C_L^c$	Circulatory lift coefficient (-)	$\dot{\alpha}$	Pitch rate ( $\text{rads}^{-1}$ )
$C_L^{nc}$	Non-circulatory lift coefficient (-)	$\alpha_0$	Zero lift angle of attack (rad)
$C_L^{rot}$	Rotational lift coefficient (-)	$\alpha_E$	Equivalent angle of attack (rad)
$C_{M_x}$	Edgewise bending moment coefficient (-)	$\beta$	Pitch angle (rad)
$C_{M_y}$	Root bending moment coefficient (-)	$\beta_g$	Geometrical pitch angle (rad)
$C_{N_\alpha}$	Linear normal force (lift) curve (-)	$\beta_p$	Operational pitch angle (rad)
$C_N^{rot}$	Rotational normal force coefficient (-)	$\Delta_\alpha^{rot}$	Rotational angle shift (rad)
$d$	Water depth (m)	$\Delta_{\alpha_1}$	Stall angle shift (rad)
$D_\alpha$	Lagged angle deficit (-)	$\eta$	Chordwise force recovery factor
$D_{ff}$	Lagged separation point deficit (-)	$\lambda$	Tip-speed ratio (-)
$E_0$	Chordwise force recovery constant (-)	$\lambda'_r$	Local instantaneous tip-speed ratio (-)
$f$	Separation point (-)	$\Omega$	Rotor rotational speed ( $\text{rads}^{-1}$ )
$f'$	Lagged separation point (-)	$\Phi$	Wagner' function (-)
$f''$	Lagged separation point (-)	$\phi$	Flow angle (rad)
$f^{rot}$	Rotational separation point (-)	$\psi$	Azimuthal position of blade (rad)
$F_D$	Drag force per unit length ( $\text{Nm}^{-1}$ )	$\rho$	Density of working fluid ( $\text{kgm}^{-3}$ )
$F_L$	Lift force per unit length ( $\text{Nm}^{-1}$ )	$\sigma$	Dummy time variable of integration (s)
$F_T$	Thrust force per unit length ( $\text{Nm}^{-1}$ )	$\tau$	Vortex transit time (-)
$F_{Tan}$	Tangential force per unit length ( $\text{Nm}^{-1}$ )	$\theta$	Phase angle of blade (rad)
$k_r$	Reduced frequency (-)	BEM	Blade element momentum
$L$	Aerodynamic loss factor (-)	D-ADP	Divergent beam Acoustic Doppler Profiler
$L_2$	Least squares error (-)	DS	Dynamic stall
$M_X$	Edgewise bending moment (Nm)	EMEC	European Marine Energy Centre
$M_Y$	Root bending moment (Nm)	LCOE	Levelised cost of energy
$N_b$	number of blades (-)	OSU	Ohio State University
$Q$	Torque acting on actuator disc (Nm)	ReDAPT	Reliable Data Acquisition Platform for Tidal
$R$	Blade tip radius (m)	SB-ADP	Single-beam Acoustic Doppler Profiler
$\dot{r}$	Reduced pitch rate constant (-)	SWL	Still water level
$r$	Blade radial coordinate (m)		

## 1. Formulation of the model

The numerical model is split into three components: determination of the angle of attack, dynamic load coefficients and rotational augmentation, which are coupled as detailed in this section. The model is available to download from our GitHub repository [1]

### 1.1. Angle of attack time history

The velocity and force components acting on a blade section are computed as shown in Figure 1 (a) and (b), respectively. The relative velocity ( $W$ ) is the magnitude of the difference between the axial velocity  $U_x(1-a)$  and the tangential velocity  $U_\psi(1+a')$ , where  $a$  and  $a'$  are the axial and tangential induction factors, respectively which account for velocities induced by the rotor wake. The angle of attack ( $\alpha$ ) is the angle that  $W$  makes with  $c$ ,  $\beta = \beta_g + \beta_p$  is the pitch angle which is measured between  $c$  and the rotor plane, where  $\beta_p$  is an operational pitch angle which may be applied to the blade. The flow angle is  $\phi = \alpha + \beta$ . The sectional drag force ( $F_D$ ) which is codirectional with

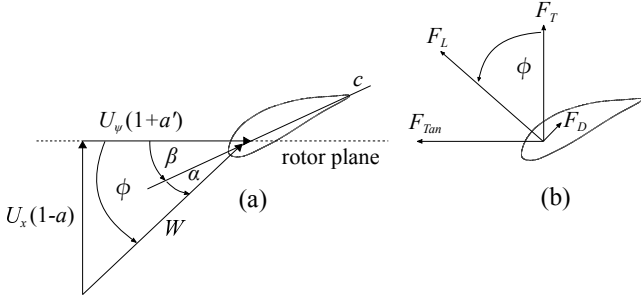


Figure 1: Blade section diagram showing (a) velocity components and (b) force components.

$W$  and the lift force ( $F_L$ ) perpendicular to it are defined per unit length as

$$F_D = \frac{1}{2} C_D \rho W^2 c, \quad F_L = \frac{1}{2} C_L \rho W^2 c, \quad (1a, b)$$

where  $C_D$  and  $C_L$  are the sectional coefficients of drag and lift, respectively and  $\rho$  is the fluid density. The axial force known as thrust ( $F_T$ ) is perpendicular to the rotor plane and is responsible for the blade bending around the  $y$ -axis known as root bending moment ( $M_Y$ ). The tangential force ( $F_{Tan}$ ) drives the turbine and causes bending around the  $x$ -axis referred to as edgewise bending moment ( $M_X$ ).  $F_T$  and  $F_{Tan}$ , expressed in terms of  $F_D$  and  $F_L$ , are

$$F_T \equiv F_L \cos \phi + F_D \sin \phi, \quad F_{Tan} \equiv F_L \sin \phi - F_D \cos \phi, \quad (2a, b)$$

which given in coefficient form are

$$C_{F_T} \equiv C_L \cos \phi + C_D \sin \phi, \quad C_{F_{Tan}} \equiv C_L \sin \phi - C_D \cos \phi. \quad (3a, b)$$

Measured D-ADP velocity data is interpolated in time ( $t$ ) and  $z$  to determine both  $U_x$  and the vertical velocity

component ( $U_z$ ) incident to each blade section for a given  $t$ . The  $z$ -coordinate of a blade section is  $z_0 + r \sin(\psi - \theta)$ , where  $\theta$  is the phase lag from the leading blade, and  $U_\psi = U_z \cos(\psi - \theta)$ .

The induction factors are initially calculated in a quasi-steady manor for one revolution using the instantaneous velocities with static  $C_L$  and  $C_D$  values to solve the BEM equations [2]. The aerodynamic forces are equated with the momentum rate of change acting on a blade annulus of width  $dr$  and position  $r$  on the blade, as shown in Figure 2. The blade-element equations are defined as

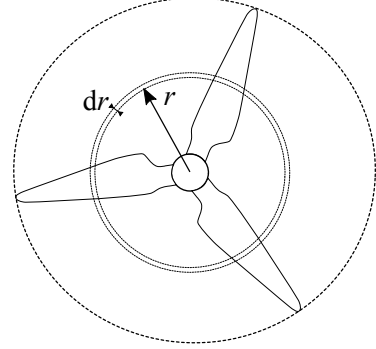


Figure 2: Incremental annulus swept out by a blade element.

$$dT = N_b \frac{1}{2} \rho W^2 C_{F_T} c dr, \quad dQ = N_b \frac{1}{2} \rho W^2 C_{F_{Tan}} c dr, \quad (4a, b)$$

where  $dT$  and  $dQ$  are the incremental thrust and torque components acting on the annulus and  $N_b$  is the number of blades. The momentum balance equations for  $dT$  and  $dQ$  are

$$dT = 4\pi r \rho U_0^2 (1-a) a L dr, \quad dQ = 4\pi r^3 \rho U_0 \Omega (1-a) a' L dr, \quad (5a, b)$$

where  $\Omega$  is the rotational velocity of the rotor and  $L$  corrects for losses due to flow leakages at the extremities of the blade where a jump in tangential velocity occurs, causing the flow to roll up into a trailing helical vortex.  $L$  is determined using Prandtl's correction for both tip and hub losses [2]. Equation 4 and Equation 5 are invalid for high induction ( $a > 0.4$ ), in this region the empirical estimation of Glauret is used with the Buhl correction [3]. The blade-element and momentum equations are equated and rearranged to give implicit definitions for  $a$  and  $a'$  which must be solved iteratively. The present model uses the solution method of Ning [4] which utilises a residual equation to converge on  $\phi$  rather than solving for both  $a$  and  $a'$ . This enables the use of a root solving algorithm which guarantees convergence. Using the geometrical definition for  $\phi$  shown in Figure 1a the following residual equation is formed

$$R(\phi) = \frac{\sin(\phi)}{(1-a)} - \frac{\cos(\phi)}{\lambda_r'(1+a')}, \quad (6)$$

where  $\lambda_r' = \frac{U_\psi}{U_x}$  is the instantaneous, local tip-speed ratio. The value of  $\phi$  which satisfies  $R(\phi) \leq 10^{-6}$  is determined

and used in the following iteration. The process is repeated until  $R(\phi) \leq 10^{-6}$ . With the induction factors determined for each time step, they are time averaged over the rotational period ( $T_r$ ). The solution to  $a$  at a point in time  $t_i$  is

$$a = \frac{1}{T_r} \int_{t_i-T_r}^{t_i} a(t) dt, \quad (7)$$

for which  $a'$  follows the same procedure. Next,  $\alpha$  time histories are calculated for each  $r$  as follows

$$\alpha(t) = \tan^{-1} \left( \frac{U_x(t)(1-a)}{U_\psi(t)(1+a')} \right) - \beta. \quad (8)$$

### 1.2. Dynamic load coefficients

The non-linear load coefficients are determined using the dynamic stall model of Sheng *et al.* [5]. This DS model is based on the 3rd generation dynamic stall model of Beddoes [6], but with a number of adaptations made to achieve better prediction at the lower Mach numbers associated with wind turbines. We modify the model to account for the effects of blade rotation and use definition for the unsteady drag coefficient given by Hansen *et al.* [7].

The total unsteady load response comprises of three elements: attached flow, trailing edge separation and leading edge vortex shedding, which we will now discuss.

#### 1.2.1. Load response in attached flow

The linear lift coefficient comprises of both circulatory and non-circulatory components. The latter accounts for flow acceleration effects, and the former for circulation around the foil and vorticity shed into the wake which introduces a phase lag and amplitude reduction from the quasi-steady value. Sheng *et al.* determine the linear solution using a method developed by Beddoes [6] which considers compressibility effects. However, for a tidal turbine the maximum Mach number is approximately 0.03, which occurs at the blade tip and is an order of magnitude less than the compressible range. Thus the attached loads are determined using the incompressible time domain solution of Wagner [8], which gives the circulatory lift coefficient ( $C_L^c$ ) to a unit step change in  $\alpha$ . The  $C_L^c$  time history for a number of arbitrary unit step changes in  $\alpha$  is determined by superposition through the Duhamel integral as follows:

$$C_L^c = 2\pi\alpha_E, \quad (9)$$

where the equivalent angle of attack that lags the physical  $\alpha$  is

$$\alpha_E = \alpha(0)\Phi(s) + \int_0^s \frac{d\alpha(\sigma)}{dt} \Phi(s-\sigma) d\sigma, \quad (10)$$

$\Phi(s)$  is the Wagner function, its argument  $s = \frac{2U_0 t}{c}$  is the non-dimensional reduced time,  $U_0$  is the freestream velocity and  $\sigma$  is a dummy time variable of integration.

Wagner does not give a convenient analytical solution to  $\Phi(s)$ . Therefore, the following exponential approximation given by Jones [9] is used

$$\Phi(s) \approx 1 - 0.1652e^{-0.0455s} - 0.335e^{-0.3s}. \quad (11)$$

The non-circulatory coefficient ( $C_L^{nc}$ ), i.e. the added mass, is treated outside of the Duhamel integral. For this term we use the approximation given by Hansen *et al.* [7], where

$$C_L^{nc} = \frac{\pi c \dot{\alpha}}{2U_0}. \quad (12)$$

Then the full lift coefficient in attached flow is  $C_L^p = C_L^c + C_L^{nc}$ . For an arbitrary  $\alpha$  forcing, Equation 9 and Equation 12 are determined numerically.

#### 1.2.2. Load response in separated flow

The first part of the non-linear solution is the load response in separated flow. To quantify this, Kirchhoff theory ([10, p. 170]) is used, which relates the position of the trailing-edge separation point to the static normal force coefficient  $C_N$ . The separation point coordinate  $x$  is normalised by the chord length ( $c$ ) giving a non-dimensional separation point  $f$ , as illustrated in Figure 3. When the boundary layer is fully attached,  $f = 1$ , and when fully separated,  $f = 0$ . The relationship between  $C_N$ ,  $\alpha$  and  $f$

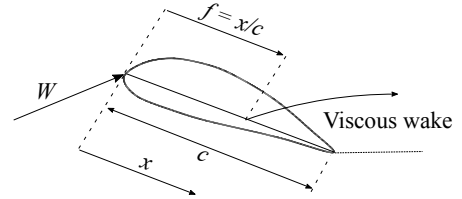


Figure 3: Trailing-edge separation point described by Kirchhoff flow past a flat plate.

is

$$C_N = C_{N_\alpha}(\alpha - \alpha_0) \left( \frac{1 + \sqrt{f}}{2} \right)^2, \quad (13)$$

where  $C_{N_\alpha} = \frac{dC_N}{d\alpha}|_{\alpha_0}$  is the slope evaluated at the angle of zero lift ( $\alpha_0$ ). Equation 13 is rearranged to solve for  $f$  using static  $C_N$  wind tunnel test data [11]. Then,  $f$  is determined for any  $\alpha$  using a look-up table. Under unsteady conditions, boundary layer separation is delayed to a higher value of  $\alpha$ . We can model this angle ( $\alpha'$ ) as a first-order lag in the  $s$  domain, namely

$$\frac{d\alpha'}{ds} = -\frac{(\alpha' - \alpha)}{T_\alpha}, \quad (14)$$

where  $T_\alpha$  is an empirical time constant describing the angle of attack delay. The solution for  $\alpha'$  is

$$\alpha' = \alpha(1 - \exp(-s/T_\alpha)). \quad (15)$$

For arbitrary forcing the exponential decay is modelled numerically with a deficit function  $D_\alpha$  such that

$$\alpha' = \alpha - D_\alpha. \quad (16)$$

Then numerically

$$D_{\alpha_j} = D_{\alpha_{j-1}} \exp\left(\frac{\Delta s}{T_\alpha}\right) + (\alpha_j - \alpha_{j-1}) \exp\left(\frac{\Delta s}{2T_\alpha}\right), \quad (17)$$

where  $j$  denotes the current time step. With  $\alpha'$  determined, the dynamic separation point  $f'$  is found using the look-up table and replacing  $\alpha$  as follows

$$f'(\alpha) = f(\alpha' - \Delta\alpha_1), \quad (18)$$

where  $\Delta\alpha_1$  is a shift delay from the static stall angle ( $\alpha_{ss}$ ).

### 1.2.3. Dynamic stall onset

To predict the angle of dynamic stall onset a linear relationship is determined between the stall onset angle ( $\alpha_{ds}$ ) and the reduced pitch rate ( $\dot{r} = \frac{\dot{\alpha}c}{2U_0}$ ) using ramp up tests [12]. Which gives

$$\alpha_{ds} = T_\alpha \dot{r} + \alpha_{ds0}. \quad (19)$$

$\alpha_{ds}$  increases linearly when  $\dot{r}$  is greater than some value  $\dot{r}_0$ , enabling a constant stall onset angle ( $\alpha_{ds0}$ ) to be obtained by extrapolating backwards from  $\dot{r}_0$  to 0. The critical onset angle is then

$$\alpha_{cr} = \begin{cases} \alpha_{ds0}, & \dot{r} \geq \dot{r}_0 \\ \alpha_{ss} + (\alpha_{ds0} - \alpha_{ss}) \frac{\dot{r}}{\dot{r}_0}, & \dot{r} < \dot{r}_0, \end{cases} \quad (20)$$

from which the delay shift from  $\alpha_{ss}$  is evaluated

$$\Delta\alpha_1 = \begin{cases} \alpha_{ds0} - \alpha_{ss}, & \dot{r} \geq \dot{r}_0 \\ (\alpha_{ds0} - \alpha_{ss}) \frac{\dot{r}}{\dot{r}_0}, & \dot{r} < \dot{r}_0. \end{cases} \quad (21)$$

Then stall onset occurs when

$$\alpha' \geq \alpha_{cr}. \quad (22)$$

### 1.2.4. Dynamic stall load response

After the onset of dynamic stall an additional lag in the separation point occurs, as the leading edge vortex forms causing an additional load overshoot. As with  $\alpha'$  a first-order lag is implemented to determine the dynamic separation point ( $f''$ )

$$\frac{df''}{ds} = -\frac{(f'' - f')}{T_v}, \quad (23)$$

where  $T_v$  is the vortex time constant which includes both the formation and convection time. The solution is again modelled with a deficit function ( $D_{ff}$ ) which describes the lag due to the dynamic vortex as

$$f'' = f' - D_{ff}, \quad (24)$$

with  $D_{ff}$  solved numerically as

$$D_{ffj} = D_{ffj-1} \exp\left(\frac{\Delta s}{T_v}\right) + (f'_j - f'_{j-1}) \exp\left(\frac{\Delta s}{2T_v}\right). \quad (25)$$

Vortex shedding follows the method of Beddoes [6], which uses a vortex shape function ( $V_x$ ) defined as follows:

$$V_x = \begin{cases} \sin^{3/2}\left(\frac{\pi\tau}{2T_v}\right), & 0 < \tau \leq T_v \\ \cos^2\left(\frac{\pi(\tau - T_v)}{T_{vL}}\right), & T_v < \tau, \end{cases} \quad (26)$$

where  $\tau$  is the non-dimensional vortex passage time which increases from zero at the onset of dynamic stall, and  $T_{vL}$  is the speed of the vortex convection. Subsequent vortex shedding occurs for  $\tau > T_v$  until the foil starts pitching down ( $\dot{r} < 0$ ) and  $V_x$  is set to zero. The additional lift contribution due to vortex shedding is then computed as the difference between the delayed and the static separation points multiplied by the shape function

$$C_N^v = B(f' - f)V_x, \quad (27)$$

where  $B$  is a constant dependent on aerofoil geometry.

### 1.2.5. Non-linear force coefficients

The final expression for the normal force coefficient  $C_N$  is

$$C_N^u = C_N^c \left(\frac{1 + \sqrt{f''}}{2}\right)^2 + C_N^{mc} + C_N^v. \quad (28)$$

The expression for the chordwise force coefficient is

$$C_C^u = \eta C_{N\alpha} (\alpha_E - \alpha_0)^2 (\sqrt{f'} - E_0), \quad (29)$$

which has no contribution from the vortex. The parameters  $\eta$  and  $E_0$  are both dependent on the sectional geometry. The lift coefficient is then

$$C_L^u = C_N^u \cos(\alpha) + C_C^u \sin(\alpha). \quad (30)$$

In the model of Sheng *et al.* the drag coefficient is defined as

$$C_D^u = C_N^u \sin(\alpha) - C_C^u \cos(\alpha) + C_{D0}, \quad (31)$$

where  $C_{D0}$  is the drag coefficient at  $\alpha_0$ , however, this definition does not bound  $C_D^u$  to the static drag curve. Therefore, we instead use the definition provided by Hansen *et al.* [13], which is expressed as three terms

$$C_D^u = C_D^{st} + C_D^{ind} + C_D^{vis}, \quad (32)$$

where

$$C_D^{ind} = C_L^u (\alpha - \alpha_E), \quad (33)$$

and

$$C_D^{vis} = (C_D^{st} - C_{D0}) \left(\frac{1 + \sqrt{f''}}{2}\right)^2 - \left(\frac{1 + \sqrt{f(\alpha_E)}}{2}\right)^2, \quad (34)$$

where  $C_D^{st}$  is the static drag coefficient determined from wind tunnel test data [11]. The three terms on the right hand side of Equation 32 are the static, induced and viscous components, respectively.  $C_D^{vis}$  is zero when the flow remains attached since  $f'' = f(\alpha_E)$ , and under near steady conditions  $C_D^{ind} \rightarrow 0$  as  $\alpha_E \rightarrow \alpha$ .

The empirical parameters for the NREL S814 are shown in Table 1. They are taken from [14], with slight modifications made using the Ohio State University (OSU) wind tunnel test data [11].

Table 1: Table of empirical parameters for the NREL S814

$\alpha_{ds0}$	0.2426
$\alpha_{ss}$	0.2007
$\alpha_0$	-0.0573
$C_{D0}$	0.01
$C_{N\alpha}$	6.267
$E_0$	0.1
$\eta$	1
$\dot{r}_0$	0
$T_\alpha$	6.33
$T_v$	4
$T_{vL}$	6
$B$	0.5
$b_1$	0.5
$b_2$	0.5

### 1.3. Rotational augmentation

Rotation of the blades induces a centrifugal force which causes a spanwise flow and a Coriolis force which accelerates the flow towards the trailing edge. These effects reduce the adverse pressure gradient to promote flow reattachment and delay separation, which in turn leads to lift augmentation from the stationary value [15]. The phenomena is not very well understood, and modelling techniques have had mixed success. The NREL Phase VI test investigated the effects of both unsteadiness and rotation on a 10 m diameter wind turbine employing NREL S809 profiles [16]. The study found that for inboard blade sections both lift and drag force are augmented compared to a non-rotating blade. However, conversely, for outer blade sections, both lift and drag are reduced. Modeling this behavior is a challenge. Breton *et al.* [17] tested the prediction capabilities of a number of rotational augmentation models to predict the NREL Phase VI test data. Their study determined that none of the models could satisfactorily predict  $C_L$  and  $C_D$  across the entire blade span, and that only the Lindenburg model [18] successfully captured a reduction in  $C_L$  at the outer sections. The Lindenburg model is well-suited to combination with the DS model since both use the separation point parameter  $f$ . To this end, we implement Lindenburg's model and combine it with the DS implementation.

The expression for the rotational lift coefficient is

$$C_L^{rot} = C_L + \frac{b_1 c}{r} \cos^2(\phi) G_1, \quad (35)$$

where  $b_1$  and  $b_2$  are empirical coefficients tuned to the NREL S809 using data from the NREL VI tests. We will use these values in our model.

$$G_1 = (1 - f)^2 \cos(\alpha^{rot}) + b_2 \cos(\alpha^{rot} - \alpha_0),$$

and  $\alpha^{rot} = \alpha + \Delta\alpha^{rot}$  is the equivalent rotational angle of attack with the following shift applied

$$\Delta\alpha^{rot} = \frac{b_1 b_2 c}{2\pi r} \cos^2(\phi). \quad (36)$$

At the outer sections ( $r \geq 0.8R$ ) where a reduction from the non-rotating lift and drag values occur  $C_{L3D}$  is given as

$$C_L^{rot} = C_L - \cos^2(\phi) \exp(-1.5AR) G_2, \quad (37)$$

where

$$G_2 = \frac{C_L(C_{N\alpha}(\alpha - \alpha_0) - 1)}{C_{N\alpha}(\alpha - \alpha_0)},$$

and AR is the aspect ratio of the outboard blade element. Lindenburg defines the rotational drag coefficient ( $C_{D3D}$ ) at all sections as

$$C_D^{rot} = C_D \frac{b_1 c}{r} \cos^2(\phi) (1 - f)^2 \sin(\alpha^{rot}), \quad (38)$$

The NREL phase VI results clearly show a reduction in the drag coefficient at the outer sections of the blade [16]. Therefore the present model will assume for  $r \geq 0.8R$ , that  $C_D^{rot} = C_D$  to avoid an over-prediction.

Using Lindenburg's theory we modify the DS model to superimpose rotational augmentation on both  $C_L^u$  and  $C_D^u$ . This is implemented by first modifying the separation point such that it is also a function of  $r$  by determining  $C_N^{rot}$  for each section and replacing  $C_N$  in Equation 13 to determine  $f^{rot}$  for each  $r$ . Then a look-up table is used to determine  $f^{rot}$  in terms of both  $\alpha$  and  $r$ . Then  $f$  in Equation 18 and Equation 27 is replaced with  $f^{rot}$ . Lastly, we apply the angle shift given by Equation 36 to both the static stall angle  $\alpha_{ss}^{rot} = \alpha_{ss} + \Delta\alpha^{rot}$ , and the critical dynamic stall onset angle  $\alpha_{ds0}^{rot} = \alpha_{ds0} + \Delta\alpha^{rot}$ .

### 1.4. Coupled blade-element momentum model

The unsteady, rotational load coefficients are coupled with the BEM model to investigate the effect on the induction factors; something which has not previously been reported in the literature.

Due to hysteresis and non-linearities,  $C_L^u(t)$  and  $C_D^u(t)$  are non-unique with  $\alpha$ . This is a problem for the BEM model which requires predefined values of  $C_L$  and  $C_D$  with  $\alpha$ . To accomodate this,  $C_L^u(t)$  and  $C_D^u(t)$  are collected from the previous time steps over the period of revolution, sorted into  $\alpha$  bins, and the mean value calculated for each bin. A smoothing spline is then applied to the points to achieve a continuous set of values. After this the Viterna deep stall extrapolation is applied [19]. This extends the coefficients  $\alpha$  range between  $-\pi$  and  $\pi$ , which is a numerical requirement of the BEM model. The look up tables, containing unique values of  $C_L^u(\alpha)$  and  $C_D^u(\alpha)$  for each  $r$  are then passed to the BEM model. New values of  $a$  and  $a'$  are determined and fed back into the numerical model, coupling the unsteady response with the induction factors. The solution is iterated until the sum of the squares error  $L_2 \leq 10^{-6}$ , where

$$L_2 = \sum_{r=r_0}^R \Delta a^2, \quad (39)$$

here  $\Delta a$  is the difference between the current and the previous value.

A flow diagram is shown in Figure 4 which illustrates the key stages and logic of the numerical model. The initial conditions first determine  $U_x$  and  $U_\psi$  as previously described, then solve  $a$  and  $a'$  for the first rotation using the static coefficients. After this  $\alpha$  and the subsequent unsteady, rotational coefficients are calculated. The coefficients are then transformed into  $C_L^u(\alpha)$  and  $C_D^u(\alpha)$ , enabling the BEM model to solve the new induction factors at each time step, which are then time averaged and fed back into the coupled model until convergence is satisfied. After which time increments by  $\Delta t$ , and the converged solution becomes the new initial condition. The process continues until the time history completes.

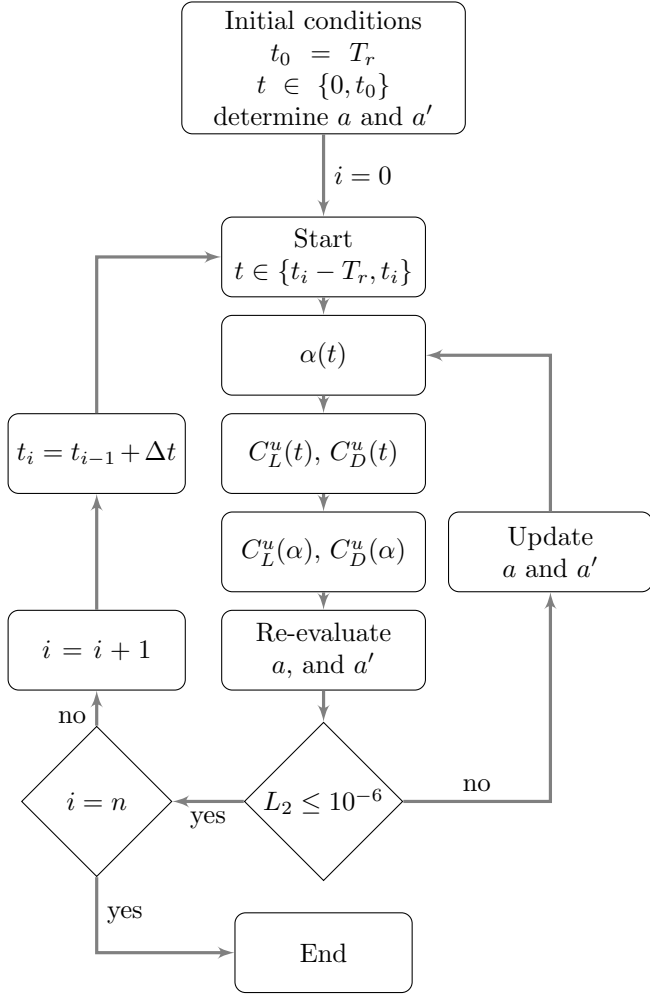


Figure 4: Process diagram of the coupled numerical model.

## 2. Validation of the model

We validated the key components of the numerical model. First the BEM implementation is used to predict values of power ( $C_P$ ) and thrust ( $C_T$ ) coefficients, respectively for a range of tip-speed ratios ( $\lambda = \frac{\Omega R}{U_0}$ )  $\in \{0.5, 8\}$ , which are compared to those predicted using AeroDyn, an open-source aerodynamic software developed by NREL, which

also uses the theoretical implementation of Ning *et al.* [20]. The turbine employs uniform thickness NREL S814 profiles at each section, the flow is steady with a current velocity of  $2.77 \text{ ms}^{-1}$ , the rotor is normal to the flow and  $\beta_p = 0$ . The results are shown in Figure 5 (a) and (b) for  $C_P$  and  $C_T$ , respectively. The predicted values of  $C_P$  are in very good agreement with that of AeroDyn up until  $\lambda = 5$ , after which the value is slightly under predicted compared to AeroDyn, although both have similarly decreasing slopes. The predicted values of  $C_T$  agree well across the full range, apart from a slight over prediction for  $\lambda \in \{4, 5\}$ . These results verify that the BEM implementation is performing as expected. Next, the predictive

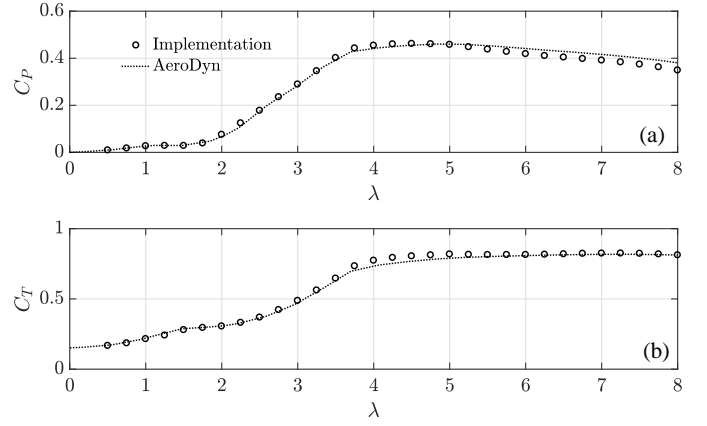


Figure 5: Power (a) and thrust (b) coefficient performance curves for a turbine operating in steady conditions.

capabilities of the DS model are tested. The relationship between  $C_L$  and  $\alpha$  for the S814 aerofoil is shown in Figure 6 for a number of cases. Empirical values from the OSU wind tunnel tests are shown for the measured static and dynamic cases [11]. Predicted values are shown for the dynamic case, and for both the static and dynamic cases with the effect of rotational augmentation. The forcing is  $\alpha = 13.8^\circ + 10.75^\circ \sin(\omega t)$ , the reduced frequency, defined  $k_r = \frac{2\pi\omega c}{W}$  is 0.091 and for the rotational case,  $r = 0.47R$ . The dynamic model predicts the value of  $C_L$  when pitching positively from around  $3^\circ$  to  $18^\circ$  very well compared to the measured dynamic data, and the shape of the load hysteresis matches qualitatively.

The model predicts the increase in lift at around  $18^\circ$  caused by vortex shedding, which leads to a peak of approximately 2.1. However, the model lags the measured value by about  $1^\circ$  leading to an over-prediction. After the peak stall occurs followed by a dramatic reduction in lift. The model predict a partial recovery from stall at around  $23^\circ$ , due to a secondary vortex being shed. The measured data follows a similar trend, with a slight recovery occurring at approximately  $22^\circ$ . During the return from stall, when  $\alpha$  is decreasing the model overpredicts  $C_L$ . Prediction in this region could be improved by using an additional return from stall model which Sheng *et al.* discuss [5], however, implementation for the type of arbitrary  $\alpha$

history caused by the wave group shown in ?? would be challenging, therefore, is not included. The modification

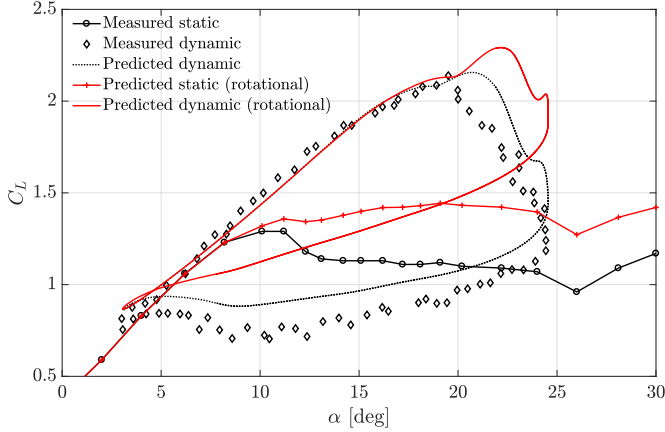


Figure 6: Lift coefficient against angle of attack for static and dynamic conditions, with and without the effect of rotation.

made to combine the effects of DS with rotational augmentation cannot easily be validated since no dynamic rotational data exists for the NREL S814. However, a qualitative comparison can be made using the NREL Phase VI experimental data for the S809. Figure 7 which has been reproduced from [21] shows the lift coefficient curve for a pitching NREL S809 foil for the rotational and non rotational cases. Here  $k_r$  is 0.1 and the location along the blade is also  $0.47R$ . The difference between the non-rotational and rotational curves for the S809 matches qualitatively with the difference between modelled dynamic and dynamic rotational curves for the S814 shown in Figure 6. The rotating foil generates a larger value of  $C_L$ , with a prominent increase due to vortex shedding visible from  $17^\circ$  to  $19^\circ$ . During the return from stall the value of  $C_L$  is approximately 50% greater for the rotational value. This confirms that dynamic lift is enhanced by rotational augmentation, and the severity, in terms of the area enclosed by the hysteresis is reduced.

The DS model agrees well quantitatively for increasing  $\alpha$ , and captures qualitatively the hysteresis shape and transient vortex shedding which characterises dynamic stall. The qualitative agreement with the rotational data for the NREL S809 suggests that the modification is sufficient to superimpose the effect of rotational augmentation on the unsteady loading.

### 3. Acknowledgements

The first named author is supported by an Engineering and Physical Sciences Research Council grant. Field measurements were acquired under the ReDAPT project (2010-2015) which was co-funded by the Energy Technologies Institute (ETI), UK.

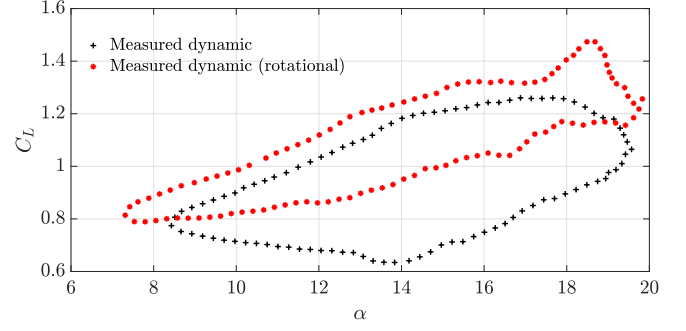


Figure 7: Unsteady lift coefficient with angle of attack for the NREL S809 aerofoil for a rotating and non-rotating aerofoil.

### References

- [1] Scarlett GT, Viola IM. Tidal turbine hydrodynamic model. 2017. URL: <https://github.com/ignaziomviola>.
- [2] Burton T, Jenkins N, Sharpe D, Bossanyi E. Wind Energy Handbook. Chichester, UK: John Wiley & Sons, Ltd; 2011. ISBN 9781119992714. URL: <http://doi.wiley.com/10.1002/9781119992714>. doi:10.1002/9781119992714.
- [3] Buhl ML. A new empirical relationship between thrust coefficient and induction factor for the turbulent windmill state. Tech. Rep. August; 2005.
- [4] Andrew Ning S. A simple solution method for the blade element momentum equations with guaranteed convergence. Wind Energy 2014;17:1327–45. URL: <http://onlinelibrary.wiley.com/doi/10.1002/we.1608/fullhttp://doi.wiley.com/10.1002/we.1636>. doi:10.1002/we.1636. arXiv:arXiv:1006.4405v1.
- [5] Sheng W, Galbraith RAM, Coton FN. A modified dynamic stall model for low Mach numbers. Journal of Solar Energy Engineering 2008;130(3):031013. URL: <http://dx.doi.org/10.1115/1.2931509http://solarenergyengineering.asmedigitalcollection.asme.org/article.aspx?articleid=1474262>. doi:10.1115/1.2931509.
- [6] Beddoes TS. A third generation model for unsteady aerodynamics and dynamic stall. Tech. Rep.; Westland Helicopters Limited; 1993.
- [7] Hansen MH, Gaunaa M, Madsen HA. A Beddoes-Leishman type dynamic stall model in state-space and indicial formulations. Tech. Rep.; 2004. URL: <http://www.risoe.dk/rispubl/vea/veapdf/ris-r-1354.pdf>.
- [8] Wagner H. Über die Entstehung des Dynamischen Auftriebes von tragflügeln. ZAMMJournal of Applied Mathematics and Mechanics/Zeitschrift für Angewandte Mathematik und Mechanik 1925;5(1):17–35.
- [9] Jones RT. The unsteady lift of a wing of finite aspect ratio. NACA Report 681 1940;doi:10.1017/CB09781107415324.004. arXiv:arXiv:1011.1669v3.
- [10] Thwaites B. Incompressible Aerodynamics: An account of the theory and observations of the steady flow of incompressible fluid past aerofoils, wings and other bodies. University Oxford Press; 1960.
- [11] Janiszewska JM, Reuss Ramsay R, Hoffmann MJ, Gregorek GM. Effects of grit roughness and pitch oscillations on the S814 airfoil. Tech. Rep.; 1996. doi:10.2172/266691.
- [12] Sheng W, Galbraith RAM, Coton FN. A new stall-onset criterion for low speed dynamic-stall. Journal of Solar Energy Engineering 2006;128(4):461. URL: <http://solarenergyengineering.asmedigitalcollection.asme.org/article.aspx?articleid=1457809>. doi:10.1115/1.2346703.
- [13] Hansen M, Sørensen J, Voutsinas S, Sørensen N, Madsen H. State of the art in wind turbine aerodynamics and aeroelasticity. Progress in Aerospace Sciences 2006;42(4):285–330. URL: <http://linkinghub.elsevier.com/retrieve/pii/S0376042106000649>. doi:10.1016/j.paerosci.2006.10.002.



- [14] Sheng W, Galbraith RAM, Coton FN. Applications of low-speed dynamic-stall model to the NREL airfoils. *Journal of Solar Energy Engineering* 2010;132(1):011006. URL: <http://solarenergyengineering.asmedigitalcollection.asme.org/article.aspx?articleid=1473733>. doi:10.1115/1.4000329.
- [15] Du Z, Selig M. The effect of rotation on the boundary layer of a wind turbine blade. *Renewable Energy* 2000;20(2):167–81. URL: <http://linkinghub.elsevier.com/retrieve/pii/S0960148199001093>. doi:10.1016/S0960-1481(99)00109-3.
- [16] Hand MM, Simms Da, Fingersh LJ, Jager DW, Cotrell JR, Schreck S, et al. Unsteady Aerodynamics Experiment Phase VI: Wind Tunnel Test Configurations and Available Data Campaigns. Tech. Rep. December; National Renewable Energy Laboratory (NREL); Golden, CO; 2001. URL: <http://www.osti.gov/servlets/purl/15000240-1FhaHo/native/>. doi:10.2172/15000240.
- [17] Breton SP, Coton FN, Moe G. A study on rotational effects and different stall delay models using a prescribed wake vortex scheme and NREL phase VI experiment data. *Wind Energy* 2008;11(5):459–82. URL: <http://doi.wiley.com/10.1002/we.269>. doi:10.1002/we.269.
- [18] Lindenburg C. Modelling of rotational augmentation based on engineering considerations and measurements. In: *European Wind Energy Conference*. 2004, p. 22–5.
- [19] Viterna L, Corrigan R. Fixed pitch rotor performance of large horizontal axis wind turbines. In: *DOE/NASA workshop on large horizontal axis wind turbines*. Cleveland, Ohio; 1981, p. 69–85.
- [20] Ning A, Hayman G, Damiani R, Jonkman JM. Development and Validation of a New Blade Element Momentum Skewed-Wake Model within AeroDyn. In: *33rd Wind Energy Symposium*. December 2014; Reston, Virginia: American Institute of Aeronautics and Astronautics. ISBN 978-1-62410-344-5; 2015; URL: <http://www.nrel.gov/docs/fy15osti/63217.pdf> <http://arc.aiaa.org/doi/10.2514/6.2015-0215>. doi:10.2514/6.2015-0215.
- [21] Guntur S, Sørensen NN, Schreck S, Bergami L. Modeling dynamic stall on wind turbine blades under rotationally augmented flow fields. *Wind Energy* 2016;19(3):383–97. URL: <http://onlinelibrary.wiley.com/doi/10.1002/we.1608/full> <http://doi.wiley.com/10.1002/we.1839>. doi:10.1002/we.1839. arXiv:arXiv:1006.4405v1.